I&EC research
Industrial & Engineering Chemistry Research

Article

Cite This: *Ind. Eng. Chem. Res.* 2018, 57, 5433−5441

pubs.acs.org/IECR

Multiscale Modeling and Simulation of Macromixing, Micromixing, and Crystal Size Distribution in Radial Mixers/Crystallizers

Cezar A. da Rosa*,† and Richard D. Braatz‡

†School of Chemistry and Food Science, Federal University of Rio Grande, FURG, Rio Grande 96201-900, Brazil

‡Massachusetts Institute of Technology, 77 Massachusetts Avenue, Cambridge, Massachusetts 02139, United States

ABSTRACT: Continuous-flow tubular crystallization in which seed crystals are continuously generated is of interest due to its enabling of tighter control of crystal properties. This article is the most detailed simulation study on the design and operation of continuous-flow crystallizers using radial mixers, which have potential for inducing rapid and intense turbulent mixing and having easy construction, high reliability, and low operating costs. A multiscale model is employed that couples computational fluid dynamics (CFD), micromixing modeling, energy balance, and population balance equation (PBE) using the open-source CFD package OpenFOAM. The approach is demonstrated for the methanol−water antisolvent crystallization of lovastatin. A new crystallizer design with multiple radial inlets is proposed and shown to deliver improved mixing compared to one radial inlet. The effects of varying operating conditions on micromixing and crystal size distribution are analyzed. A systematic approach is provided for the design of continuous-flow tubular crystallizers with radial mixing.

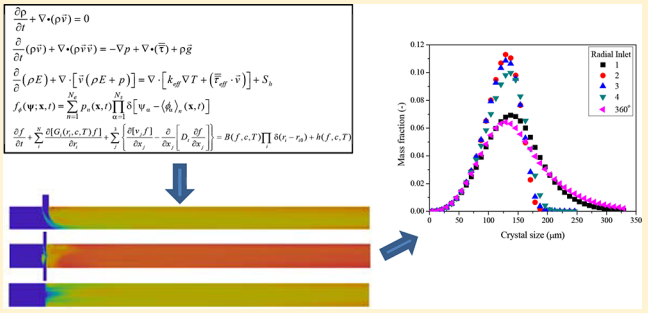

1. INTRODUCTION

Crystallization is widely used in the chemical and pharmaceutical industries to perform solid−liquid separation and purification to produce high-value materials such as pharmaceuticals, catalysts, and pigments.[1] Several crystallizer designs and crystallization techniques have been applied in order to obtain products with high purity and desired crystal size distribution (CSD).[2,3]

Among various methods of crystallization used, especially by the pharmaceutical industry, the mixing of a liquid solution containing the desired solute with a miscible antisolvent to reduce the solubility has the advantage of inducing crystallization of thermally sensitive pharmaceuticals without large temperature variations.[1,4] Since the solubility of the solute in the antisolvent is very low, supersaturation is quickly induced, creating a driving force for crystallization. Since this method requires rapid and sufficient mixing of the antisolvent with the solute dissolved in solvent, the design and optimization of such crystallizers play an important role in achieving crystallization with effective control of the CSD.[5]

Many different antisolvent mixer designs have been explored to obtain high supersaturation in order to generate consistent crystal nuclei that are subsequently grown to a desired size.[6−10] Over the past decade, state-of-the-art mixers/crystallizers such as impinging jet and coaxial nozzles have gained more attention.[5,11−14] The radial mixer is an alternative that is largely unknown in crystallization applications but is widely used as a thermal mixer in nuclear power plants, chemical plants, and combustors.[15−17] Its success in inducing intense turbulent mixing in other applications suggests that the radial mixer has potential in antisolvent crystallization due to its easy construction, reliability, and low operating costs. However, the use of the radial mixer in antisolvent crystallization applications, which is referred to here as a *radial crystallizer*, is limited by a lack of information regarding design and operation for that purpose.

Although numerous experimental studies have been carried out to gain a better understanding of the operation of antisolvent crystallizers,[18−24] the number of possible designs and operating conditions that can be investigated is large. As such, performing bench-scale experiments over the variety and range of possibilities can be time-consuming and costly. The application of mathematical modeling including transport phenomena to such complex systems as radial crystallizers can facilitate the search for more efficient processes, to improve the production capacity, reduce operating costs, and identify potential operational problems such as fouling on the pipe walls. In addition, the detailed modeling and simulation of these processes enable the analysis and a building of understanding of variables that are difficult to measure experimentally, such as the spatial variation of extent of mixing and nucleation and growth rates.

In this regard, Woo et al.[13,25] applied an isothermal single-phase model with constant properties coupled with micromixing models, the Reynolds-averaged Navier−Stokes equation, and a spatially varying population balance equation using a high-resolution central difference discretization scheme to simulate the behavior of batch and impinging jet antisolvent crystallizers.

Received: January 23, 2018
Revised: March 28, 2018
Accepted: April 2, 2018
Published: April 2, 2018

DOI: 10.1021/acs.iecr.8b00359
Ind. Eng. Chem. Res. 2018, 57, 5433−5441

Pirkle et al.[5] extended the model and software of Woo et al.[13,25] to account for the nonisothermal operation of antisolvent crystallizers and studied the effect of different operating conditions in the behavior of a coaxial nozzle crystallizer. Such detailed investigations have not been published for radial crystallizers.

The objective of this work is to investigate different radial antisolvent crystallizer designs and operating conditions and to improve the performance of this type of crystallizer via mathematical modeling and numerical simulations. A single-phase model with variable properties coupled with the Fox[26] micromixing model, a population balance equation using a high-resolution finite-volume method, an energy balance, and scalar transport equations was implemented in the open-source CFD package OpenFOAM. The methanol−water antisolvent crystallization of lovastatin, using kinetics reported in the literature,[27] was chosen as the model system in the simulations. The influence of different numbers of radial inlets and operating conditions in the micromixing, crystal size distribution (CSD), and solute conversion was investigated.

2. MODEL EQUATIONS

This article employs a multiscale mathematical modeling approach that couples the dynamic Reynolds-averaged Navier−Stokes equations with a multienvironment probability density (PDF) model[26] that captures the micromixing in the subgrid scale, a population balance equation (PBE) that models the evolution of the crystal size distribution, and the energy balance equation to account for the heat transfer between the solvent and antisolvent, as well as the heat of mixing and crystallization.

2.1. Conservation of Mass and Momentum Equations.

The macromixing was modeled by the Reynolds-averaged Navier−Stokes (RANS) model and the standard $k-\varepsilon$ turbulence model with enhanced wall treatment. In order to incorporate the effect of density difference between the solution and antisolvent, an ideal mixture model was employed to calculate the mixture density at every computational grid cell. In general form, the equations are

$$\text{continuity equation:}\quad \frac{\partial \rho}{\partial t} + \nabla\cdot(\rho\vec{v}) = 0 \tag{1}$$

momentum conservation equation:

$$\frac{\partial}{\partial t}(\rho\vec{v}) + \nabla\cdot(\rho\vec{v}\vec{v}) = -\nabla p + \nabla\cdot(\bar{\bar{\tau}}) + \rho\vec{g} \tag{2}$$

standard $k-\varepsilon$ equations:

$$\frac{\partial}{\partial t}(\rho k) + \nabla\cdot(\rho k\vec{v}) = \nabla\cdot\left[\left(\mu + \frac{\mu_t}{\sigma_k}\right)\nabla\cdot k\right] + G_k - \rho\varepsilon + S_k$$

$$\frac{\partial}{\partial t}(\rho\varepsilon) + \nabla\cdot(\rho\varepsilon\vec{v}) = \nabla\cdot\left[\left(\mu + \frac{\mu_t}{\sigma_\varepsilon}\right)\nabla\cdot\varepsilon\right] + C_{1\varepsilon}\frac{\varepsilon}{k}G_k - C_{2\varepsilon}\rho\frac{\varepsilon^2}{k} + S_\varepsilon$$

$$\mu_t = \rho C_\mu \frac{k^2}{\varepsilon} \tag{3}$$

The symbols are defined in the Nomenclature list.

2.2. Micromixing Model Equations.

As in Marchisio et al.,[28−30] Woo et al.,[13,25] and Pirkle et al.,[5] the micromixing effects were considered by applying the finite-mode PDF model proposed by Fox.[26] In this approach, each computational cell in the CFD grid is divided into N_e different probability modes or environments, which correspond to a discretization of the presumed composition PDF into a finite set of delta (δ) functions:

$$f_\phi(\psi;\mathbf{x},t) = \sum_{n=1}^{N_e} p_n(\mathbf{x},t)\prod_{\alpha=1}^{N_s}\delta[\psi_\alpha - \langle\phi_\alpha\rangle_n(\mathbf{x},t)] \tag{4}$$

where f_ϕ is the joint PDF of all scalars, N_s is the total number of scalars (species), p_n is the probability of mode n or volume fraction of environment n, and $\langle\phi_\alpha\rangle_n$ is the mean composition of scalar α corresponding to mode n. The weighted concentration is defined as

$$\langle\mathbf{s}\rangle_n \equiv p_n\langle\phi\rangle_n \tag{5}$$

The transport of probability and species in inhomogeneous flows is modeled by

$$\frac{\partial\mathbf{p}}{\partial t} + \sum_i\left[\langle v_i\rangle\frac{\partial\mathbf{p}}{\partial x_i} - \frac{\partial}{\partial x_i}\left(D_t\frac{\partial\mathbf{p}}{\partial x_i}\right)\right] = \mathbf{G}(\mathbf{p}) + \mathbf{G_s}(\mathbf{p}) \tag{6}$$

$$\frac{\partial\langle\mathbf{s}\rangle_n}{\partial t} + \sum_i\left[\langle v_i\rangle\frac{\partial\langle\mathbf{s}\rangle_n}{\partial x_i} - \frac{\partial}{\partial x_i}\left(D_t\frac{\partial\langle\mathbf{s}\rangle_n}{\partial x_i}\right)\right] = \mathbf{M}^n(\mathbf{p},\langle\mathbf{s}\rangle_1,\ldots,\langle\mathbf{s}\rangle_{N_e}) + \mathbf{M}_\mathbf{s}^n(\mathbf{p},\langle\mathbf{s}\rangle_1,\ldots,\langle\mathbf{s}\rangle_{N_e}) + p_n\mathbf{S}(\langle\phi\rangle_n) \tag{7}$$

where $\mathbf{G}$ and $\mathbf{M}^n$ are the rates of change of $\mathbf{p} = [p_1, p_2, \ldots, p_N]$ and $\langle\mathbf{s}\rangle_n$ due to micromixing, respectively; $\mathbf{G_s}$ and $\mathbf{M}_\mathbf{s}^n$ are additional micromixing terms to eliminate the spurious dissipation rate in the mixture-fraction-variance transport equation (see Fox[26] for details); and $\mathbf{S}$ is the chemical source term. The conservation of probability requires that

$$\sum_{n=1}^{N} p_n = 1 \tag{8}$$

and

$$\sum_{n=1}^{N_e} G_n(\mathbf{p}) = 0 \tag{9}$$

The mean compositions of the scalars are given by

$$\langle\phi\rangle = \sum_{n=1}^{N_e} p_n\langle\phi\rangle_n = \sum_{n=1}^{N_e}\langle\mathbf{s}\rangle_n \tag{10}$$

and since the means remain unchanged by micromixing,

$$\sum_{n=1}^{N_e}\mathbf{M}^n(\mathbf{p},\langle\mathbf{s}\rangle_1,\ldots,\langle\mathbf{s}\rangle_{N_e}) = 0 \tag{11}$$

must be satisfied. In this article, a three-environment model was chosen to account for the micromixing effects. In this approach, the solution of solute/solvent is the environment 1, the antisolvent represents the environment 2, and the mixture of environments 1 and 2 forms the environment 3. According to Marchisio et al.,[28−30] the use of three environments is sufficient to capture the micromixing effects in nonpremixed flows with satisfactory accuracy.

Following Fox,[26] the micromixing terms for the three-environment model are summarized in Table 1, where the values of $\langle\boldsymbol{\varphi}\rangle_n = \langle\mathbf{s}\rangle_n/p_n$ denote the unweighted variables. The

DOI: 10.1021/acs.iecr.8b00359
Ind. Eng. Chem. Res. 2018, 57, 5433−5441

Table 1. Micromixing Terms

model variable	G, $\mathbf{M}^n$	$\mathbf{G}_s$, $\mathbf{M}_s^n$
p_1	$-\gamma p_1(1-p_1)$	$\gamma_s p_3$
p_2	$-\gamma p_2(1-p_2)$	$\gamma_s p_3$
p_3	$\gamma[p_1(1-p_1)+p_2(1-p_2)]$	$-2\gamma_s p_3$
$\langle \mathbf{s} \rangle_3$	$\gamma[p_1(1-p_1)\langle\varphi\rangle_1 + p_2(1-p_2)\langle\varphi\rangle_2]$	$-\gamma_s p_3\,(\langle\varphi\rangle_1 + \langle\varphi\rangle_2)$
$\gamma = \frac{\varepsilon_\xi}{p_1(1-p_1)(1-\langle\xi\rangle_3)^2 + p_2(1-p_2)\langle\xi\rangle_3^2}$		
$\gamma_s = \frac{2D_t}{(1-\langle\xi\rangle_3)^2 + \langle\xi\rangle_3^2}\frac{\partial\langle\xi\rangle_3}{\partial x_i}\frac{\partial\langle\xi\rangle_3}{\partial x_i}$		
$\langle\xi'^2\rangle = p_1(1-p_1) - 2p_1p_3\langle\xi\rangle_3 + p_3(1-p_3)\langle\xi\rangle_3^2$		

scalar dissipation rate (ε_ξ) was calculated according to Pirkle et al.,[5] and mixture fractions in environments 1 and 2 are $\langle\boldsymbol{\xi}\rangle_1 = 1$ and $\langle\boldsymbol{\xi}\rangle_2 = 0$, respectively.

2.3. Population Balance Equation. In order to account for the spatially inhomogeneous crystallization, a population balance equation (PBE),

$$\frac{\partial f}{\partial t} + \sum_i^N \frac{\partial[G_i(r_i,c,T)f]}{\partial r_i} + \sum_j^3 \left\{ \frac{\partial[v_j f]}{\partial x_j} - \frac{\partial}{\partial x_j}\left[D_t \frac{\partial f}{\partial x_j} \right] \right\} = B(f,c,T)\prod_i \delta(r_i - r_{i0}) + h(f,c,T) \tag{12}$$

was used.[31] The PBE is a continuity statement expressed in terms of the particle number density function f, which is a function of external coordinates (X, Y, and Z in the Cartesian 3D case), internal coordinates r_i which are the size dimensions of the crystals, and time t.

In the PBE (eq 12), the rates of growth G_i and nucleation B are functions of the vector of solution concentrations c and the temperature T, δ is the Dirac delta function, and h describes the creation and destruction of crystals due to aggregation, agglomeration, and breakage. For size-dependent growth, the rates of growth G_i also varies with the r_i.

The PBE (eq 12), discretized along the crystal growth axis using high-resolution finite volume method,[25] was rewritten on a mass basis and solved as a set of scalar transport equations in the CFD solver:

$$f_{w,j} = \rho_c k_v \int_{r_{j-1/2}}^{r_{j+1/2}} r^3 f_j \, dr = \frac{\rho_c k_v f_j}{4}\left[(r_{j+1/2})^4 - (r_{j-1/2})^4 \right] \tag{13}$$

$$\frac{\partial}{\partial t} f_{w,j} + \sum_i^3 \left\{ \frac{\partial[v_j f_{w,j}]}{\partial x_i} - \frac{\partial}{\partial x_i}\left[D_t \frac{\partial f_{w,j}}{\partial x_i} \right] \right\} = \begin{cases} \frac{\rho_c k_v}{4\Delta r}[(r_{j+1/2})^4 - (r_{j-1/2})^4]\left\{ -G_{j+1/2}\left[f_j + \frac{\Delta r}{2}(f_r)_j \right] + G_{j-1/2}\left[f_{j-1} + \frac{\Delta r}{2}(f_r)_{j-1} \right] + B_{j=0} \right\}; & \Delta c > 0 \\ \frac{\rho_c k_v}{4\Delta r}[(r_{j+1/2})^4 - (r_{j-1/2})^4]\left\{ -G_{j+1/2}\left[f_{j+1} - \frac{\Delta r}{2}(f_r)_{j+1} \right] + G_{j-1/2}\left[f_j - \frac{\Delta r}{2}(f_r)_j \right] \right\}; & \Delta c < 0 \end{cases} \tag{14}$$

where $f_{w,j}$ is the cell-averaged crystal mass and has the units kg/m^3, $\Delta r = r_{j+1/2} - r_{j-1/2}$, ρ_c is the crystal density, k_v is the crystal volume shape factor, $(f_r)_j$ is the derivative approximated by the minmod limiter,[32] and Δc is the supersaturation.

2.4. Conservation of Energy Equation. In order to apply the energy balance, the three environments are assumed to be in thermal equilibrium at the cell level. This assumption is based on the time required to achieve thermal equilibrium in a turbulent flow at the cell level, which is, in a worst-case scenario, the same order of magnitude as the cell residence time. Also, compressibility effects are neglected since the fluids are in the liquid phase. Thus, the general form of the energy equation can be written as

$$\frac{\partial}{\partial}(\rho E) + \nabla\cdot[\vec{v}(\rho E + p)] = \nabla\cdot[k_{\text{eff}}\nabla T + (\bar{\bar{\tau}}_{\text{eff}}\cdot\vec{v})] + S_h$$

$$E = h - \frac{p}{\rho} + \frac{v^2}{2} \tag{15}$$

where k_{eff} is the effective conductivity and the source term (S_h) accounts for the heat of crystallization and heat of mixing between methanol and water in environment 3,

$$S_h = S_3(-\Delta H_{\text{mix}}) + \left(\sum_j S_{f_{w,j}} \right)(-\Delta H_{\text{crys}}) \tag{16}$$

where S_3 ($\mathbf{M}^n + \mathbf{M}_s^n$) is the rate of increase in the concentration of solvent + antisolvent in environment 3, ($\sum_j S_{f_{w,j}}$) is the rate of increase in total crystal mass in environment 3, ΔH_{mix} is the heat of mixing of methanol with water in mass basis, and ΔH_{crys} is the heat of crystallization of lovastatin from a methanol−water mixture in mass basis. The values of ΔH_{mix} depend on the mas fraction of methanol in the mixture and are taken from Bertrand et al.[32] The heat of crystallization ΔH_{crys} is derived from a van't Hoff relation used to fit the solubility data (see next section).

2.5. Crystallization Kinetics of Lovastatin. Following the work of Pirkle et al.,[5] the solubility and nucleation and growth rates for lovastatin are calculated from

$$c^* \text{ (kg/kg of solvents)} = 0.001 \exp(15.45763(1 - 1/\theta))\left\{ \begin{array}{l} -(2.7455\times10^{-4})W_{as}^3 + (3.3716\times10^{-2})W_{as}^2 - \\ \quad 1.6704W_{as} + 33.089, \text{ for } W_{as} \le 45.67 \\ -(1.7884\times10^{-2})W_{as} + 1.7888, \text{ for } W_{as} > 45.67 \end{array} \right\}$$

$$\theta = \frac{T}{T_{\text{ref}}}, \quad T_{\text{ref}} = 296 \text{ K} \tag{17}$$

$$B = B_{\text{homogeneous}} + B_{\text{heterogeneous}}$$

$$B_{\text{homogeneous}} \text{ at } 23\ ^\circ\text{C } (\#/(\text{s}\cdot\text{m}^3)) = 6.97\times10^{14}\exp\left(\frac{-15.8}{[\ln S]^2} \right)$$

$$B_{\text{heterogeneous}} \text{ at } 23\ ^\circ\text{C } (\#/(\text{s}\cdot\text{m}^3)) = 2.18\times10^{8}\exp\left(\frac{-0.994}{[\ln S]^2} \right) \tag{18}$$

$$G \text{ at } 23\ ^\circ\text{C (m/s)} = (8.33\times10^{-30})(2.46\times10^3 \ln S)^{6.7} \tag{19}$$

where W_{as} is the weight percent of antisolvent (H_2O), $S = c/c^*$ is the relative supersaturation, and c and c^* are the solution and saturated concentration, respectively, and the coefficient 15.45763 in the temperature-dependence factor infers a heat of crystallization value of $-\Delta H_{\text{crys}} = 38\,042.5$ kJ/kmol. The solubility (eq 17) was fit to experimental data from three sources cited by ref 5, whereas the nucleation and growth rate expressions

DOI: 10.1021/acs.iecr.8b00359
Ind. Eng. Chem. Res. 2018, 57, 5433−5441

(eqs 18 and 19 are from an early experimental study on antisolvent crystallization.[24]

3. NUMERICAL SOLUTION PROCEDURE

3.1. Computational Domain. The effect of the number of radial inlets was investigated by creating five different 3D computational domains, with $XYl_{z=0}$ plane of symmetry, with one, two, three, and four radial inlets, as well as a 360° radial inlet, as illustrated in Figure 1 for four radial inlets. In all of the

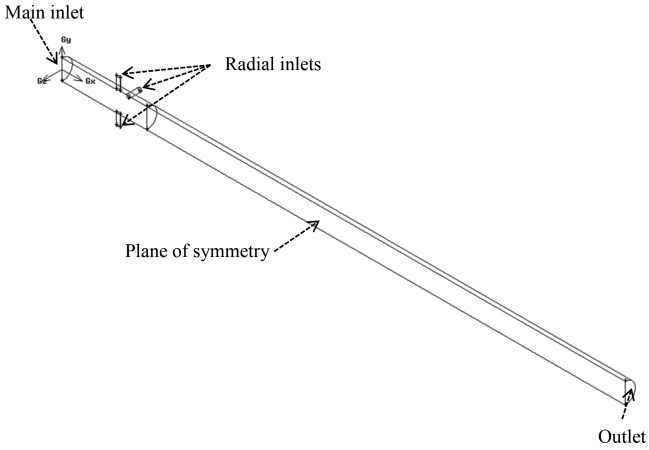

Figure 1. Illustration of the computational domains used in the simulations.

domains, the diameter and length of the main pipe were 0.0363 and 1 m, respectively. The radial inlets were positioned at an axial position of $X = 0.1$ m. In order to keep the same specific kinetic energy and total mass flow rate at the radial inlets, the area of the inlets was calculated according to the number of inlets considered.

3.2. Mesh. The numerical solutions were performed on 3D computational meshes. GAMBIT 2.13 software was used to set up the computational grid, and the fluentMeshToFoam tool, which is available in OpenFOAM, was used to convert the grid to OpenFOAM standards. Triangular and rectangular cell faces were used, when needed, to improve the mesh quality. The average grid spacing between nodes was set to 1 mm.

3.3. Model Implementation and Numerical Solution. The model equations were implemented on OpenFOAM 2.3 via object-oriented C++ programing language. A set of dictionaries was used to input the transport, PBE, and finite-mode PDF properties and variables. The population balance equation was discretized into 30 bins for the longest growth axis, with $\delta r = 8$ μm. The 30 semidiscretized PBE equations, resulting from PBE growth axis discretization, were implemented in OpenFOAM code using the PtrList<T> C++ template which constructs an array of classes or templates of type T. The merged PISO-SIMPLE (PIMPLE) algorithm was applied to run the simulations. This algorithm combines the SIMPLE algorithm and then uses pressure implicit with splitting the operators (PISO) algorithm to rectify the second pressure correction and correct both velocities and pressure explicitly.[33] The schemes implemented for both convection divergence and diffusion (Laplacian) terms were the bounded second-order linear upwind and the unbounded second-order linear limited differencing schemes, respectively. Transient simulations were run until the solutions achieved the steady state. Grid-independent numerical solutions were obtained by comparing the steady-state solution for different grid sizes.

3.4. Operating Conditions Studied Here. Simulations were performed with the solution of lovastatin/methanol (solute/solvent) fed through the main inlet at a temperature of 305 K, and the antisolvent (pure water) was fed through the radial inlet at a temperature of 293 K. In all the simulations, the total mass flow rate (solution + antisolvent) was kept constant and equal to 1.0 kg/s which corresponds to an approximate average residence time of 1.0 s.

First, the effect of taking into account the heat of mixing and the heat of crystallization in the temperature and consequently in the CSD and solute conversion was analyzed. After that, different radial inlet configurations and radial inlet velocities were studied. In this first set of simulations the methanol/water mass flow ratio was set to 1.0. Further, the influence of methanol/water inlet mass flow ratio on the mixing properties and crystallization was analyzed for the best radial inlet configuration.

4. RESULTS AND DISCUSSION

4.1. Effect of Heat of Mixing and Heat of Crystallization on Temperature and CSD. In order to analyze the effect of heat of mixing and heat of crystallization separately, three simulations were performed: (a) without considering the heats of mixing and crystallization; (b) only considering the heat of crystallization; (c) considering both heat of mixing and heat of crystallization. The spatial temperature fields and mass-weighted outlet CSDs for these simulations are shown in Figures 2 and 3, respectively.

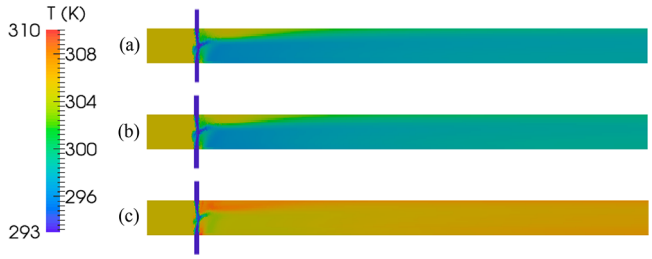

Figure 2. Temperature contour plot: (a) no heat of mixing and crystallization; (b) only heat of crystallization; (c) heat of mixing and crystallization.

The inclusion of the heat of crystallization term in the simulations, as expected for the system studied here, does not affect the temperature significantly (Figure 2b), with the average outlet temperature being 298.6 K compared to 298.1 K when the term is not included (Figure 2a). The heat of mixing, on the other hand, strongly affects the spatial distribution of temperature in the crystallizer (cf. Figure 2a,b and Figure 2c), with an average outlet temperature of 306.2 K. The heat of mixing also notably affects the CSD, as shown in Figure 3, with a narrower CSD and much smaller mean crystal size compared to simulations in which the heat of mixing is not taken into account. The solute conversion into crystals is affected by the heat of mixing, reducing its value from 81.5% for simulation (a) to 70.4% for simulation (c). The higher temperatures caused by the heat of mixing result in higher solubility (eq 17) and lower supersaturation and growth and nucleation rates (eqs 18 and 19), which together result in both lower solute conversion and lower mean crystal size (Figure 3a).

DOI: 10.1021/acs.iecr.8b00359
Ind. Eng. Chem. Res. 2018, 57, 5433−5441

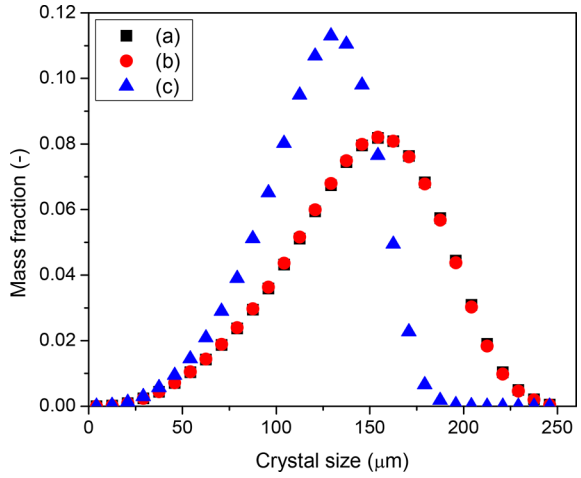

Figure 3. Mass-weighted average CSD calculated at the outlet: (a) no heat of mixing and crystallization; (b) only heat of crystallization; (c) heat of mixing and crystallization.

4.2. Results for Different Radial Inlet Configurations. As mentioned before, the effect of different radial inlet configurations on micromixing and CSD was analyzed. Figures 4 and 5

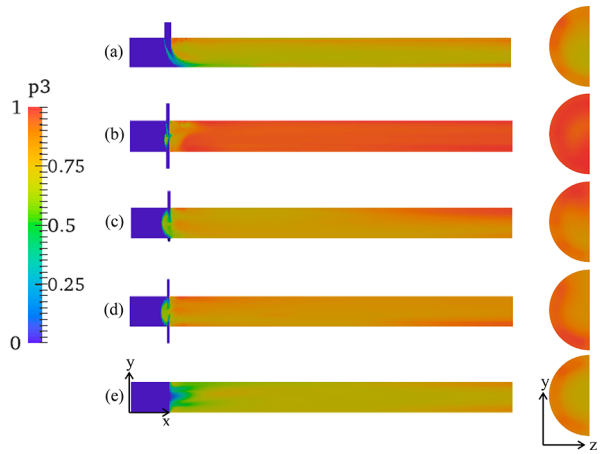

Figure 4. Volume fraction of the mixed environment (p_3): (a) one radial inlet; (b) two radial inlets; (c) three radial inlets; (d) four radial inlets; (e) 360° radial inlet.

show the results for the volume fraction of the mixed environment (p_3) and CSD at the outlet for the five different configurations. In order to make a comparison, the velocity at the inlets, the mass flow rates of methanol and water, and the residence time were kept constant in all the cases.

As shown in Figure 4 and Table 2, increasing the number of radial inlets from one to two improved the micromixing of the crystallizer; however, further increments in the number of radial inlets had a negative effect on the micromixing, reducing p_3 values. Also, the configuration with two radial inlets showed a more uniform mixture at the outlet when compared to the other configurations studied here, as can be observed in the $YZ|_{x=1}$ plane cut in Figure 4. This behavior can be explained by the high turbulence intensity generated by the two impinging jets found in the configuration with two radial inlets. On the other hand, when more jets are introduced, this effect is attenuated and the turbulence of the mixture is decreased. Under these conditions, the single radial inlet results in the axial and radial feeds

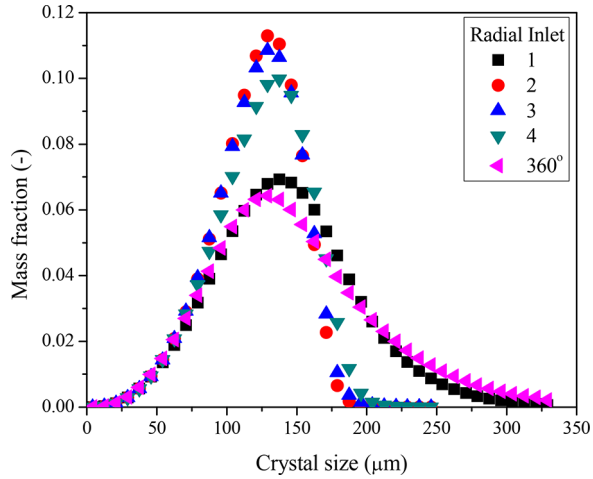

Figure 5. Mass-weighted average CSD calculated at the outlet for different radial inlet configurations.

Table 2. Area-Averaged p_3, Average Crystal Size, and Solute Conversion, Calculated at the Outlet, for Different Radial Inlet Configurations

radial inlet	p_3 (−)	average crystal size (μm)	solute conversion (%)
1	0.81	143	55.4
2	0.97	120	70.4
3	0.89	121	63.9
4	0.88	125	58.7
360°	0.85	147	56.1

interacting at the lower wall (Figure 4a), which indicates a higher potential for fouling than seen for larger numbers of radial inlets.

The number of inlets also played an important role in the CSD and solute conversion, as observed in Figure 5 and Table 2. Higher values of p_3 (better micromixing) generated smaller crystals with narrower CSD, as well as higher solute conversions. Although the solute conversion is different, the normalized outlet CSDs for two, three, and four inlets are similar (Figure 5). The nonmonotonic dependency of the CSD on the number of inlets resulted in the outlet CSDs being similar for one and an infinite number of inlets (marked as 360° in Figure 5). Since the configuration with two radial inlets produced the higher solute conversion and fastest mixing, further analysis was performed only for this case.

4.3. Effect of Different Radial Inlet Velocities on Crystallizer Performance. As expected, increasing the radial inlet velocity increases the turbulence intensity which leads to a better micromixing, as observed in Figures 6 and 7a and Table 3.

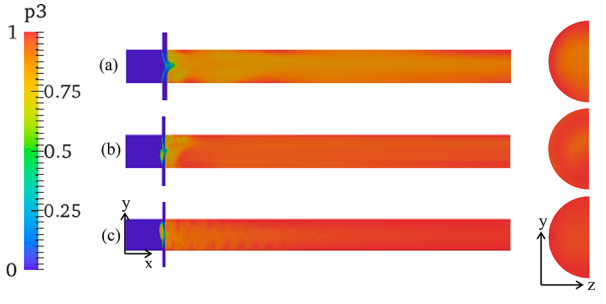

Figure 6. Volume fraction of the mixed environment (p_3) for different radial inlet velocities: (a) 2 m/s; (b) 4 m/s; (c) 6 m/s.

DOI: 10.1021/acs.iecr.8b00359
Ind. Eng. Chem. Res. 2018, 57, 5433−5441

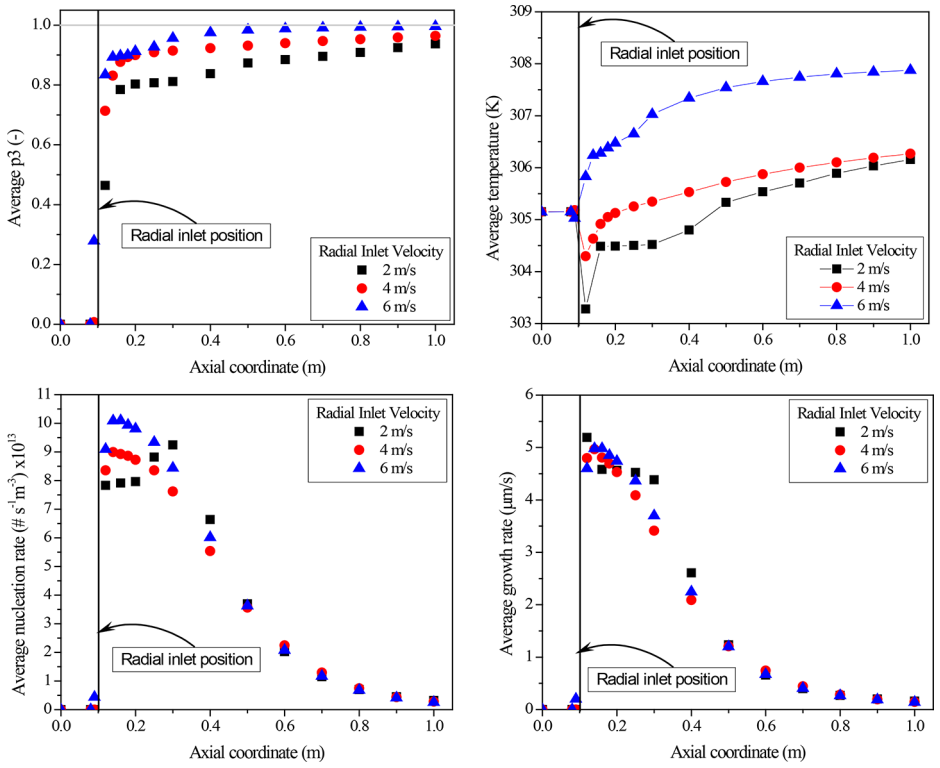

Figure 7. Mass-weighted average variables as a function of the axial coordinate calculated for different radial inlet velocities: (a) volume fraction of the mixed environment; (b) temperature distribution; (c) nucleation rate; (d) growth rate.

Table 3. Area-Averaged p_3, Average Crystal Size, and Solute Conversion, Calculated at the Outlet, for Different Radial Inlet Velocities

inlet velocity (m/s)	p_3 (−)	average crystal size (μm)	solute conversion (%)
2	0.94	124	68.2
4	0.97	120	70.4
6	1.00	114	71.7

The increased turbulence intensity and micromixing (i.e., higher values of p_3) as higher radial inlet velocity leads to higher temperatures in the crystallizer in nearly all axial positions along the crystallizer, as observed in Figure 7b.

If the temperature was constant, improving micromixing would lead to higher volumetric crystal growth and nucleation rates. However, the higher temperature associated with improved micromixing increases the solubility (eq 17) and reduces supersaturation and, consequently, reduces the volumetric crystallization rates (eqs 18 and 19). The opposing effects of micromixing mean that the nucleation and growth rates can be higher or lower at any particular axial position (Figure 7c,d). Near the radial inlet position, the effect of the radial velocity on the nucleation rate (Figure 7c) is stronger than for the growth rate (Figure 7d). Although the simulation with a radial velocity of 6 m/s showed superior micromixing, the crystal growth rate is similar to the other radial velocities (Figure 7d). The higher overall nucleation rate with similar growth rate explains the narrower CSD (Figure 8) and higher solute conversion (Table 3) obtained at higher radial inlet velocity.

4.4. Effect of Solvent/Antisolvent Mass Flow Ratio on Crystallization. The effect of the solvent/antisolvent mass flow ratio on the crystallizer operation was investigated while maintaining the total mass flow (1 kg/s), the radial inlet velocity

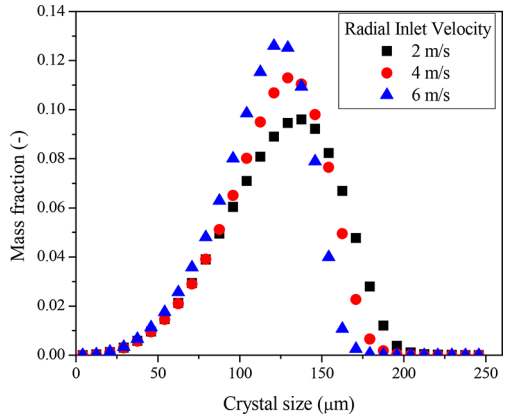

Figure 8. Mass-weighted average CSD at the outlet for different radial inlet velocities.

(6 m/s), and the residence time constant. The smaller methanol/water mass flow ratios showed somewhat improved micromixing right after the radial inlet position ($X = 0.1$ m), but all achieved $p_3 \approx 1.0$ at the axial position around 0.8 m (Figure 9a). While better micromixing was observed to generate higher temperature due to the heat of mixing in the previous sections, this trend was not observed when the better micromixing was generated by reducing methanol/water mass flow ratio (Figure 9b). The heat of mixing of Bertrand et al.[32] is a nonlinear function of the methanol mass fraction that has a maximum value at a mass fraction of 0.37, which leads to higher absolute heat of mixing values for the smaller mass flow ratios studied here. In spite of this, the simulation with a methanol/water mass flow ratio of 0.66 showed lower temperature values when compared to the mass flow ratios of 1.00 and 1.50. The lowest methanol/water mass flow ratio of 0.66 also had the lowest average feed temperature, as

DOI: 10.1021/acs.iecr.8b00359
Ind. Eng. Chem. Res. 2018, 57, 5433−5441

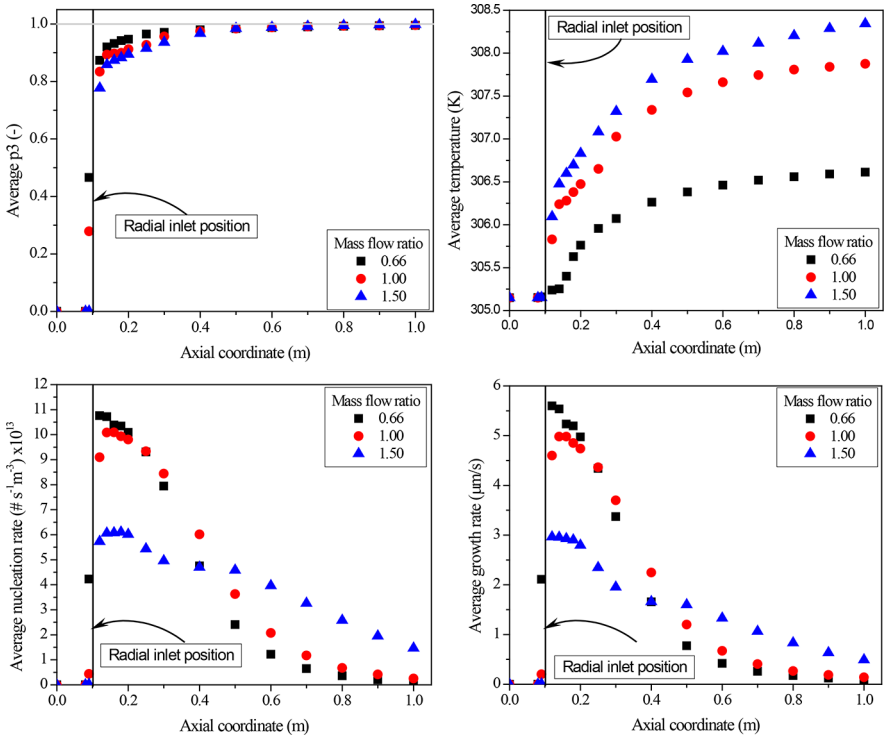

Figure 9. Mass-weighted average variables as a function of the axial coordinate calculated for different mass flow ratios: (a) volume fraction of the mixed environment; (b) temperature distribution; (c) nucleation rate; (d) growth rate.

the streams of methanol and water are fed at 305 and 293 K, respectively. The different temperatures of the feed streams of methanol and water had a stronger effect on the temperature distribution in Figure 9b than the heat of mixing effect.

The smaller methanol/water mass flow ratios had higher nucleation and growth rates near the radial inlet position (Figure 9c,d). Although the concentration of lovastatin in the resulting solvent/antisolvent mixture is higher for the mass flow ratio of 1.50, the nucleation and growth rates are the lowest, which is caused by both higher temperatures and lower water mass fraction, which reduces the supersaturation. These relationships also explain the trend for solute conversion, which is 75.1%, 71.7%, and 44.5% for 0.66, 1.00, and 1.50 mass flow ratios, respectively. The average outlet crystal size and CSD were similar for the mass flow ratios and so are not reported here.

4.5. Evolution of the Crystal Size Distribution. One of the advantages of using the discrete PBE is the ability to predict the full crystal size distribution at every grid cell, which enables a better understanding of the crystallization process and the definition of an optimum residence time to produce a desired CSD. In order to represent this ability and further analyze the behavior of the antisolvent crystallization of lovastatin in a radial crystallizer, the mass-weighted average CSD was plotted for different axial positions, as shown in Figure 10. The data presented here were obtained for a radial inlet velocity of 6 m/s and a methanol/water mass flow ratio equal to 1.

The low crystal concentration and high supersaturation, observed near the radial inlet position (0.10 m), make the nucleation the dominant phenomenon for low contact time, which explains the narrower CSD and smaller average crystal size observed for the axial positions up to 0.20 m. After that, as the crystals concentration increase with increasing contact time, the growth phenomenon becomes dominant, which produces

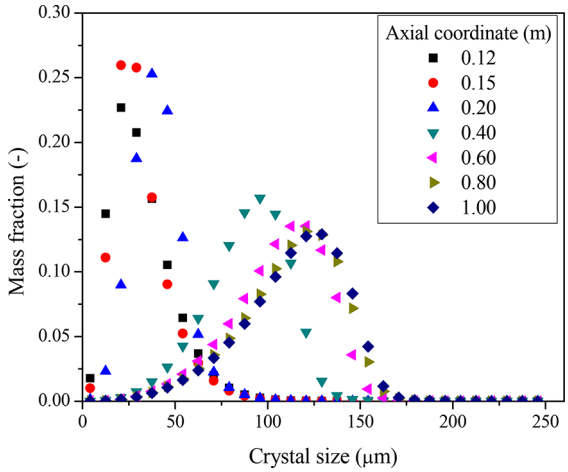

Figure 10. Mass-weighted average crystal size distribution obtained for different axial positions.

broader CSD and higher average crystal size, as observed in Figure 10.

4.6. Comparison with a Past Study of the Effectiveness of Radial Mixers for Particle Formation. To our knowledge, the only other study to simulate the effects of mixing for a radial mixer that produces particles is the application of CFD to the precipitation of barium sulfate.[34] Precipitation is a form of reactive crystallization in which two solutions are mixed to generate a salt that has very low solubility, so crystals nucleate and grow. Both processes form particles and are influenced by micromixing. While both studies employed the RANS model coupled to some form of a particle formation model, our simulation model is more general in that it includes the effects of micromixing and simulates a full population balance model rather than a method-of-moments model.[34] Wei and Garside[34]

DOI: 10.1021/acs.iecr.8b00359
Ind. Eng. Chem. Res. 2018, 57, 5433−5441

reported that turbulent mixing and particle formation yields in the radial mixer were much higher than the coaxial mixer, which was consistent with past experimental studies and supports the physical intuition that higher difference in the initial momenta leads to higher mixing. That is, better mixing is achieved by a radial mixer, which has the inlet velocities of the radial pipe in a different direction (perpendicular) to the inlet velocities of the main feed pipe, than a coaxial mixer, which has the inlet velocities of both feed streams in the same direction (downstream). The past study[34] only considered a single radial inlet, whereas our study considered multiple inputs. In our study, we show that the use of two opposing radial inlet pipes results in significantly higher turbulent mixing and partial formation yields than using a single radial inlet pipe. These results are consistent with the physical intuition that higher difference in the initial momenta leads to higher mixing. That is, better mixing is achieved by have two radial inlet pipes with inlet velocities that oppose each other, which maximizes the norm of the difference between the average momenta of the two radial feed streams than when having a single radial inlet pipe in which all of the inlet momenta vectors are in the same direction. This two-radial-pipe configuration has the advantage of higher mixing intensity, without having the geometric restrictions used in most dual impinging jet mixer designs.[13]

5. CONCLUSION

A single-phase Reynolds-averaged Navier−Stokes model with variable properties coupled with a micromixing model, population balance equation, energy balance, and scalar transport equations is successfully implemented in the open-source CFD package OpenFOAM. This model is applied to study the methanol/water antisolvent crystallization of lovastatin in radial mixers/crystallizers. The simulation results in this article demonstrate that the heat of mixing plays an important role in the energy balance for the studied system. Also, the design of the radial inlet is studied and a new configuration with two impinging jets is proposed and found to be the best among the radial configurations, showing superior results for micromixing, CSD, and solute conversion. In the case study, increasing the radial inlet velocity improves the micromixing and the solute conversion and generates a narrower CSD. In addition, micromixing and the crystal nucleation and growth rates are higher near the radial inlet position for a methanol/water mass flow ratio of 0.66 than higher values.

AUTHOR INFORMATION

Corresponding Author

*E-mail: darosacezar@gmail.com. Phone: 55-53-3293-5370.

ORCID

Cezar A. da Rosa: 0000-0003-2164-5943

Richard D. Braatz: 0000-0003-4304-3484

Notes

The authors declare no competing financial interest.

NOMENCLATURE

B = nucleation rate [#/(m^3·s)]
c = concentration of solute [kg/m^3 or kg/kg]
c^* = solubility or saturation concentration [kg/m^3 or kg/kg]
Δc = supersaturation [kg/m^3 or kg/kg]
D, D_m = diffusion coefficient or laminar diffusivity [m^2/s]
D_t = turbulent diffusivity [m^2/s]
f = number density function [#/(m_c·m^3)]
f_r = derivative of number density function [#/(m_c^2·m^3)]
f_w = mass density function [kg/(m_c·m^3)]
f_ϕ = joint probability function of all scalars
$\vec{g}$ = gravitational acceleration [m/s^2]
G = growth rate [m/s]
$\mathbf{G}(\mathbf{p})$ = rate of change of $\mathbf{p}$ = [p_1 p_2 ... p_{Ne}] due to micromixing
$\mathbf{G_s}(\mathbf{p})$ = term to eliminate spurious dissipation rate in eq [12]
h = enthalpy per unit mass, J/kg
k = turbulent kinetic energy [m^2/s^2] in turbulence and micromixing equations Boltzmann's constant in nucleation rate expression
k_v = volume shape factor
$\mathbf{M}^n$ = rate of change of $\langle \mathbf{s} \rangle_n$ due to micromixing
$\mathbf{M}_s^n$ = term to eliminate spurious dissipation rate in eq [13]
N = number of particle size cells or bins
N_e = number of probability modes or environments
p = pressure [Pa] in momentum conservation equation
p_n = probability of mode n or volume fraction of environment n in micromixing model
r = crystal size [m]
r_0 = nuclei size [m]
Δr = Discretized bin size for crystal size [m]
Re = Reynolds number
$\langle \mathbf{s} \rangle_n$ = weighted concentration of mean composition of scalars ϕ in mode n
S = relative supersaturation = c/c^*
S_{as} = user defined source term of antisolvent concentration [kg/(m^3·s)]
S_ε = user defined source term for dissipation rate of turbulent kinetic energy
S_k = user defined source term for turbulent kinetic energy
t = time [s]
T = temperature [°C]
$\vec{v}$ = Velocity vector [m/s]
W_{as} = antisolvent mass percent [%]

Special Units

m = length unit (m) in mixer/crystallizer
m_c = length unit (m) in crystal
m_3 = length unit (m) in environment 3

Symbols

Δc = supersaturation = $c - c^*$
ε = turbulent kinetic energy dissipation rate [m^2/s^3]
ε_ξ = scalar dissipation rate [1/s]
φ = volume fraction of solids in effective viscosity expression
φ_k = scalar
$\langle \phi \rangle$ = mean composition of scalar in environment
ρ_3 = fluid density of environment 3
μ = viscosity [kg/(m·s)]; effective viscosity of suspension [kg/(m·s)] in effective viscosity expression
μ_t = turbulent viscosity [kg/(m·s)]
θ = constant in minmod limiter
ρ = density [kg/m^3]
ρ_c = crystal density [kg/m^3]
τ = stress tensor [kg/(m·s^2)]
ν = kinematic viscosity [m^2/s]
$\langle \xi \rangle$ = mixture fraction
$\langle \xi'^2 \rangle$ = mixture fraction variance

Subscripts

i = crystal dimension in population balance equation; instance for dropping seed crystals
c = denotes crystal property

DOI: 10.1021/acs.iecr.8b00359
Ind. Eng. Chem. Res. 2018, 57, 5433−5441

j = discretized bin for crystal size in population balance equation
n = environment in micromixing model

REFERENCES

(1) Mullin, J. W. *Crystallization*; Elsevier Butterworth-Heineman: Oxford, U.K., 2001.
(2) McCabe, W. L.; Smith, J. C.; Harriot, P. *Unit Operations of Chemical Engineering*, 7th ed.; McGraw-Hill: New York, 2004.
(3) Nowee, S. M.; Abbas, A.; Romagnoli, J. A. Model-Based Optimal Strategies for Contolling Particle Size in Antisolvent Crystallization Operation. *Cryst. Growth Des.* **2008**, *8*, 2698.
(4) Wey, J. S.; Karpinski, P. H. Batch Crystallization. In *Handbook of Industrial Crystallization*; Butterworth-Heinemann: Boston, MA, 2002.
(5) Pirkle, C., Jr.; Foguth, L. C.; Brenek, S. J.; Girard, K.; Braatz, R. D. Computational fluid dynamics modeling of mixing effects for crystallization in coaxial nozzles. *Chem. Eng. Process.* **2015**, *97*, 213.
(6) Fujiwara, M.; Nagy, Z. K.; Chew, J. W.; Braatz, R. D. J. First Principles and direct design approaches for the control of pharmaceutical crystallization. *J. Process Control* **2005**, *15*, 493.
(7) Dauer, R.; Mokrauer, J. E.; McKeel, W. J. U.S. Patent 5578279, 1996.
(8) Lindrud, M. D.; Kim, S.; Wei, C. U.S. Patent 6302958, 2001.
(9) am Ende, D. J.; Crawford, T. C.; Weston, N. P. U.S. Patent 6558435, 2003.
(10) Wang, X.; Gillian, J. M.; Kirwan, D. J. Quasi-emulsion precipitation of pharmaceuticals. 1. conditions for formation and crystal nucleation and growth behavior. *Cryst. Growth Des.* **2006**, *6*, 2214.
(11) Lindrud, M. D.; Kim, S.; Wei, C. U.S. Patent 6302958 B1, 2001.
(12) Hacherl, J. M.; Paul, E. L.; Buettner, H. M. Investigation of impinging-jet crystallization with a calcium oxalate model system. *AIChE J.* **2004**, *49*, 2352.
(13) Woo, X. Y.; Tan, R. B. H.; Braatz, R. D. Modeling and computational fluid dynamics-population balance equation-micromixing simulation of impinging jet crystallizers. *Cryst. Growth Des.* **2009**, *9*, 156.
(14) Öncül, A. A.; Sundmacher, K.; Seidel-Morgenstern, A.; Thévenin, D. Numerical and analytical investigation of barium sulphate crystallization. *Chem. Eng. Sci.* **2006**, *61*, 652.
(15) Kickhofel, J.; Valori, V.; Prasser, H. M. Turbulent penetration in T-junction branch lines with leakage flow. *Nucl. Eng. Des.* **2014**, *276*, 43.
(16) Gao, K.; Wang, P.; Lu, T.; Song, T. Experimental investigation and numerical simulation for weakening the thermal fluctuations in a T-junction. *Ann. Nucl. Energy* **2015**, *78*, 180.
(17) Kartaev, E. V.; Emelkin, V. A.; Ktalkherman, M. G.; Aulchenko, S. M.; Vashenko, S. P.; Kuzmin, V. I. Formation of counter flow jet resulting from impingement of multiple jets radially injected in a crossflow. *Exp. Therm. Fluid Sci.* **2015**, *68*, 310.
(18) Mahajan, A. J.; Kirwan, D. J. Micromixing effects in a two-impinging-jets precipitator. *AIChE J.* **1996**, *42*, 1801.
(19) Doki, N.; Kubota, N.; Yokota, M.; Kimura, S.; Sasaki, S. J. Production of sodium chloride crystals of uni-modal size distribution by batch dilution crystallization. *J. Chem. Eng. Jpn.* **2002**, *35*, 1099.
(20) Kaneko, S.; Yamagami, Y.; Tochihara, H.; Hirasawa, I. J. Effect of supersaturation on crystal size and number of crystals produced in antisolvent crystallization. *J. Chem. Eng. Jpn.* **2002**, *35*, 1219.
(21) Falcon, J. A.; Berglund, K. A. Monitoring of antisolvent addition crystallization with raman spectroscopy. *Cryst. Growth Des.* **2003**, *3*, 947.
(22) Borissova, A.; Dashova, Z.; Lai, X.; Roberts, K. J. Examination of the semi-batch crystallization of benzophenone from saturated methanol solution via aqueous antisolvent drowning-out as monitored in-process using ATR FTIR spectroscopy. *Cryst. Growth Des.* **2004**, *4*, 1053.
(23) An, J. H.; Kim, W. S. Antisolvent crystallization using ionic liquids as solvent and antisolvent for polymorphic design of active pharmaceutical ingredient. *Cryst. Growth Des.* **2013**, *13*, 31.
(24) Park, M. W.; Yeo, S. D. Antisolvent crystallization of carbamazepine from organic solutions. *Chem. Eng. Res. Des.* **2012**, *90*, 2202.
(25) Woo, X. Y.; Tan, R. B. H.; Chow, P. S.; Braatz, R. D. Simulation of mixing effects in antisolvent crystallization using a coupled CFD-PDF-PBE approach. *Cryst. Growth Des.* **2006**, *6*, 1291.
(26) Fox, R. O. *Computational Models for Turbulent Reacting Flows*; Cambridge University Press: Cambridge, U.K., 2003.
(27) Mahajan, A. J.; Kirwan, D. J. Nucleation and growth kinetics of biochemicals measured at high supersaturations. *J. Cryst. Growth* **1994**, *144*, 281.
(28) Marchisio, D. L.; Barresi, A. A.; Fox, R. O. Simulation of turbulent precipitation in a semi-batchtaylor-couette reactor using CFD. *AIChE J.* **2001**, *47*, 664.
(29) Marchisio, D. L.; Fox, R. O.; Barresi, A. A.; Baldi, G. On the comparison between presumed and full PDF Methods for turbulent precipitation. *Ind. Eng. Chem. Res.* **2001**, *40*, 5132.
(30) Marchisio, D. L.; Fox, R. O.; Barresi, A. A.; Garbero, M.; Baldi, G. On the simulation of turbulent precipitation in a tubular reactor via computational fluid dynamics (CFD). *Chem. Eng. Res. Des.* **2001**, *79*, 998.
(31) Randolph, A. D.; Larson, M. A. *Theory of Particulate Processes*; Academic Press Inc.: San Diego, CA, 1988.
(32) Bertrand, G. L.; Millero, F. J.; Wu, C.-H.; Hepler, L. G. Thermochemical investigations of the water-ethanol and water-methanol solvent systems. I. Heats of mixing, heats of solution, and heats of ionization of water. *J. Phys. Chem.* **1966**, *70*, 699.
(33) Versteeg, H.; Malalasekera, W. *An Introduction to Computational Fluid Dynamics: The Finite Volume Method*; Longman Scientific & Technical: Harlow, U.K., 1995.
(34) Wei, H.; Garside, J. Application of CFD modeling to precipitation systems. *Trans. IChemE* **1997**, *75*, 219.

DOI: 10.1021/acs.iecr.8b00359
Ind. Eng. Chem. Res. 2018, 57, 5433−5441